An analysis of the pre-, co-, and post-seismic effects of the 2024 Noto Earthquake and Tsunami

Saeed Mohanna[1]; Lingsen Meng[1]; Alessandro Vuan[2]; Tung-Cheng Ho[3], Chao An[4], Liuwei Xu[1]

[1]University of California, Los Angeles (saeedmohanna@g.ucla.edu), [2]Istituto Nazionale di Oceanografia e di Geofisica Sperimentale, [3]Kyoto University, [4]Shanghai Jiao Tong University

Motivation

- With 299 fatalities, the 2024 New Year's Day earthquake and subsequent tsunami that struck the Noto Peninsula was the deadliest since the 2011 Tohoku earthquake and tsunami.
- Resolving the coseismic slip using a combination of tsunami, SAR-derived deformation and GNSS data can paint a more comprehensive picture of the rupture of the mainshock.
- Obtaining a more complete catalog of seismicity to analyze its spatiotemporal evolution can better illuminate the physical drivers of this earthquake.

Methods

Source inversion

1) Static inversion [1] of tsunami, SAR-derived 3D-deformation and GNSS data to obtain slip and rake values on modified fault geometry from [2].

2) Adjoint inversion ([3], [4]) of tsunami data.

- No assumptions of fault geometry needed
- Relies on time-reversal imaging [5] to obtain an initial estimate for the initial water elevation of the tsunami source.
- Initial estimate is updated using a form of gradient descent to minimize the gradient of the L2-norm misfit between observations and predictions. The gradient is equivalent to the adjoint wavefield itself.

Seismicity detection and relocation

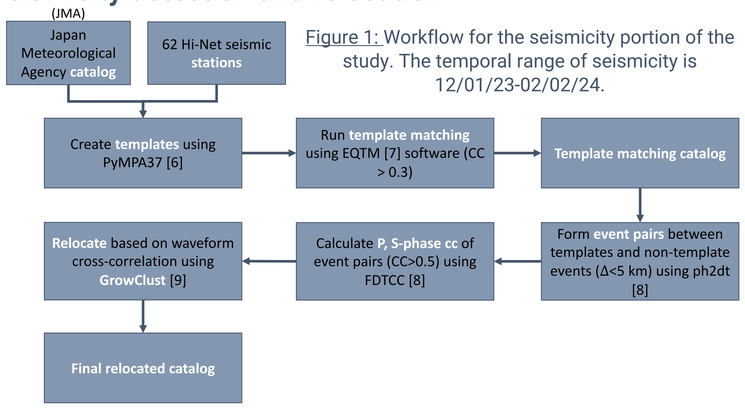

Figure 1: Workflow for the seismicity portion of the study. The temporal range of seismicity is 12/01/23-02/02/24.

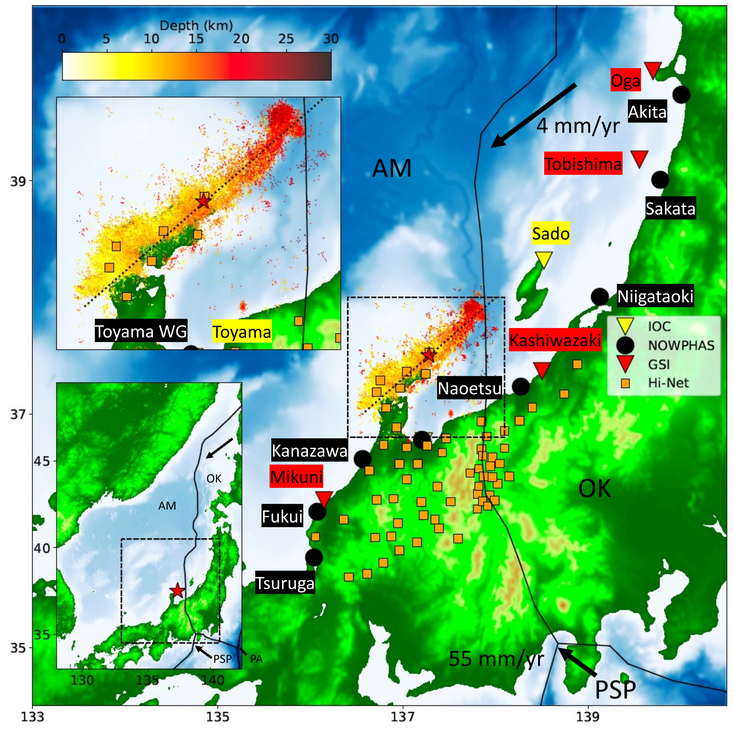

Figure 2: Map showing an overview of the study area, station locations and seismicity results. Figure legend shows the names of various agencies the stations were obtained from. Inverted triangles are tide gauges, circles are water gauges and squares are seismometers. OK=Okhotsk Plate, AM=Amur Plate, PSP=Philippine Sea Plate, PA=Pacific Plate.

Results

Static inversion

Slip and seafloor deformation

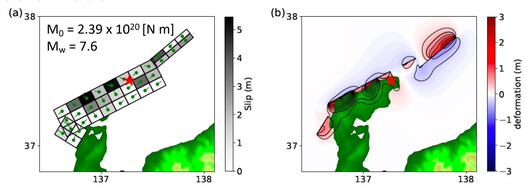

Figure 3: (a) Coseismic slip model with rakes shown (green arrows) and (b) associated seafloor deformation.

Geodetic data (VR_{SAR} = 76%, weight = 0.1; VR_{GNSS} = 65%, weight = 1)

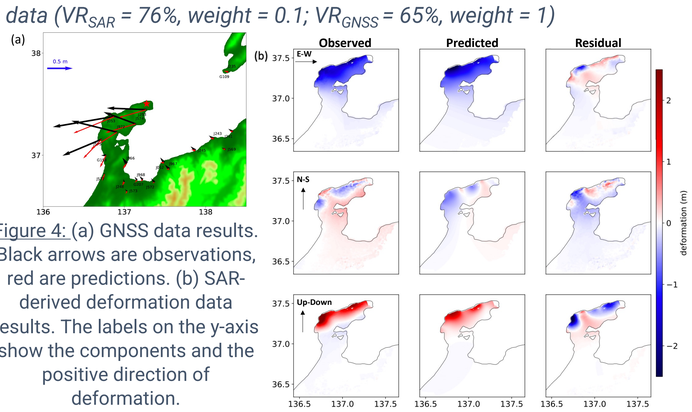

Figure 4: (a) GNSS data results. Black arrows are observations, red are predictions. (b) SAR-derived deformation data results. The labels on the y-axis show the components and the positive direction of deformation.

Tsunami data ($VR_{Tsunami}$ = 72%, weight = 0.3)

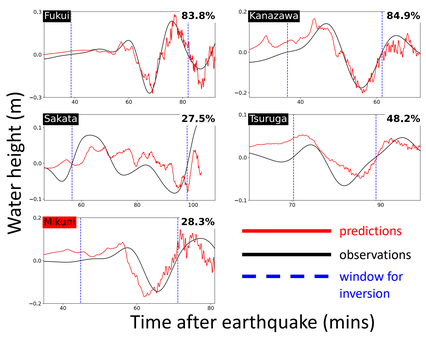

Figure 5: Results of the tsunami stations used in the inversion. Number in the upper right corner of each plot corresponds to the variance reduction (VR) of each station. Each station shown was given a weight of 1 in the inversion.

Dataset weights were chosen by finding the combination of weights that achieves the highest average VR across the 3 datasets.

A smoothing parameter of 0.3 was chosen by finding the value with the highest average VR when using the best dataset weight combination.

Adjoint inversion

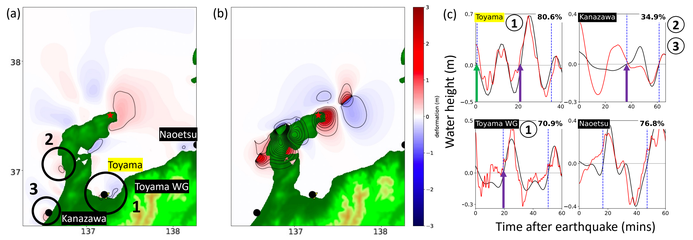

Figure 6: (a) Initial water elevation after 50 iterations of the adjoint inversion. Areas highlighted with thick solid black circles and numbers indicate possible landslide sources examined in our validation analysis in (c). (b) Seafloor deformation from a tsunami-only static inversion. Contours in (a) and (b) are in intervals of 0.25 m. (c) waveform fitting of (a) to some of the stations used in the inversion. These plots have the same legend as that of Figure 5. Green arrows on selected stations show the arrival time of a landslide-induced tsunami wave. Purple arrows show the arrival time of the earthquake-induced tsunami wave. Stations examined for landslide signals have a circle marked with the candidate landslide number. The $VR_{Tsunami}$ was ~76% for the adjoint inversion.

Analysis

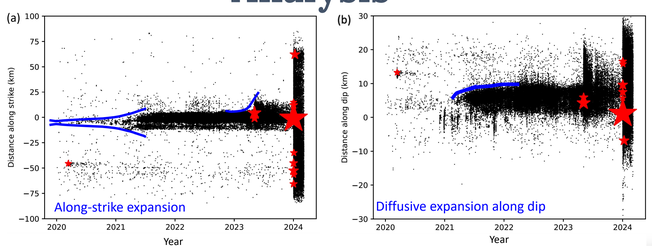

Figure 7: Spatiotemporal evolution of seismicity from the JMA catalog along (a) strike and (b) dip of the black dotted line in Figure 2 from 01/01/2020-03/06/2024. Modified from [10].

Acknowledgments

This work is supported by the National Science Foundation's award number 1848486.

Analysis continued

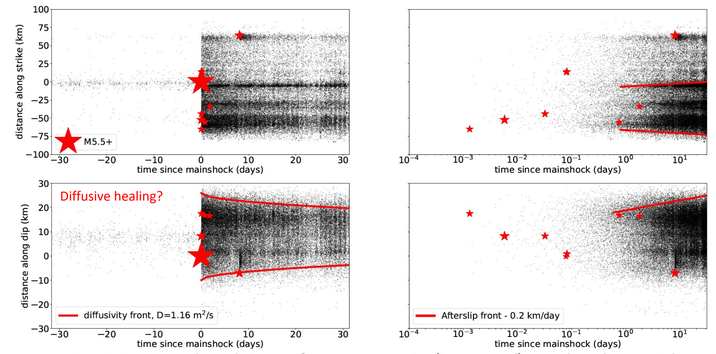

Figure 8: Spatiotemporal evolution of our seismicity (top panel) results along strike and (bottom panel) dip (angle = 41°) of the black dotted line in Figure 2. The plots on the right show a log scale on the horizontal axis.

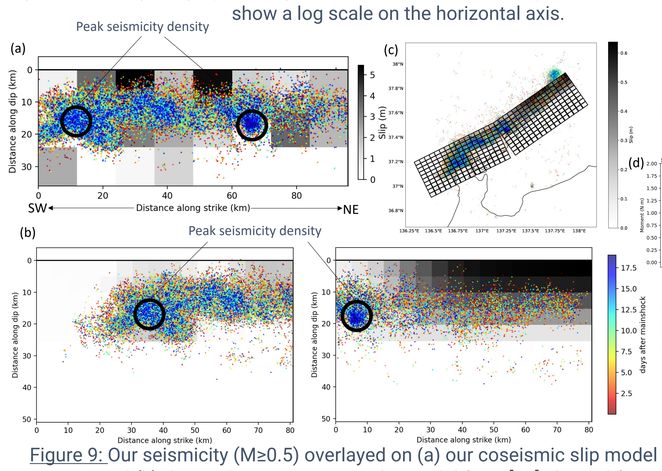

Contrast in calculated moments for the NE segment!

Potential aseismic process occurring on the NE segment, where the earthquakes are deeper

Figure 9: Our seismicity (M≥0.5) overlayed on (a) our coseismic slip model presented in Figure 3a and (b) the 19-day post-seismic slip model from [11], derived from geodetic data. (c) Map view of (b) with (d) showing a comparison of the geodetically-derived moment to seismicity-derived moment across the SW and NE fault segments.

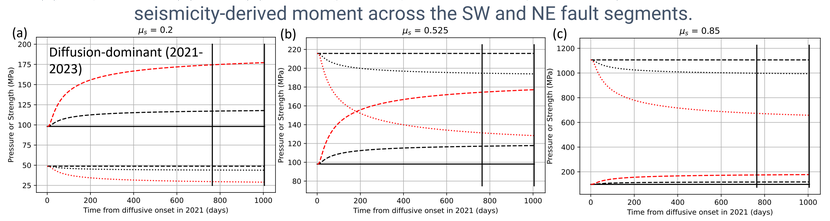

Figure 10: Temporal evolution of fault strength and pore fluid pressure [12] 1 km along the dip from the injection point in the 2021 swarm at a depth of 10 km for various coefficients of static friction (a, b, c) and pore fluid pressure coefficients. Vertical solid black lines show the time of the 2023 and 2024 earthquakes. Fault strength changes are shown in the table below.

Time Frame/Friction	μ_s = 0.2	μ_s = 0.525	μ_s = 0.85
2021-2023 (avg. annual)	~3-10 MPa	~11-43 MPa	~54-217 MPa
2023-2024	~0.2-0.7 MPa	~0.7-2.9 MPa	~3.7-15 MPa

Conclusions

- The mainshock ruptured multiple fault segments along the Noto Peninsula, including a deeper offshore fault with a dip angle of 70°.
- Adjoint inversion of tsunami data suggests a submarine landslide occurred in Toyama Bay.
- Template matching and earthquake relocation reveal afterslip along both strike and dip. Fluid diffusion along dip seems to follow a healing front as opposed to the typical expansion associated with swarm activity.

References

[1] Lawson, C. L., & Hanson, R. J. (1995). Solving least squares problems. Society for Industrial and Applied Mathematics.
[2] Ma, Z., et al. (2024). Slow rupture in a fluid-rich fault zone initiated the 2024 M_w 7.5 Noto earthquake. Science 385, 866-871. https://doi.org/10.1126/science.ado5143
[3] Zhou, T., Meng, L., Xie, Y., & Han, J. (2019). An adjoint-state full-waveform tsunami source inversion method and its application to the 2014 Chile-Iquique tsunami event. Journal Of Geophysical Research: Solid Earth, 124, 6737–6750. https://doi.org/10.1029/2018JB016678
[4] Xie, Y., Mohanna, S., Meng, L., Zhou, T., & Ho, T.-C. (2023). Adjoint inversion of near-field pressure gauge recordings for rapid and accurate tsunami source characterization. Earth and Space Science, 10, e2023EA003086. https://doi.org/10.1029/2023EA003086
[5] Hossen, M.J., Cummins, P.R., Roberts, S.G. et al. (2015). Time Reversal Imaging of the Tsunami Source. Pure and Applied Geophysics. 172, 969–984. https://doi.org/10.1007/s00024-014-1014-5
[6] Vuan, A., Sugan, M., Amati, G., Kato, A. (2018). Improving the Detection of Low-Magnitude Seismicity Preceding the M_w 6.3 L'Aquila Earthquake: Development of a Scalable Code Based on the Cross Correlation of Template Earthquakes. Bulletin of the Seismological Society of America. 108 (1): 471–480. https://doi.org/10.1785/0120170106
[7] Vuan, A. (2024). EQTM. GitHub. https://github.com/avuan/EQTM.git
[8] Waldhauser, F., Ellsworth, W. (2000). A Double-Difference Earthquake Location Algorithm: Method and Application to the Northern Hayward Fault, California. Bulletin of the Seismological Society of America. 90 (6): 1353–1368. https://doi.org/10.1785/0120000006
[9] Trugman, D., Shearer, P. (2017). GrowClust: A Hierarchical Clustering Algorithm for Relative Earthquake Relocation, with Application to the Spanish Springs and Sheldon, Nevada, Earthquake Sequences. Seismological Research Letters. 88 (2A): 379–391 https://doi.org/10.1785/0220160188
[10] Peng, Z., Lei, X., Wang, Q.Y., Wang, D., Mach, P., Yao, D., Kato, A., Obara, K., Campillo, M. (2024) The Evolution Process between the Earthquake Swarm Beneath the Noto Peninsula, Central Japan and the 2024 M 7.6 Noto Hanto Earthquake Sequence, Earthquake Research Advances, 100332, ISSN 2772-4670, https://doi.org/10.1016/j.eqrea.2024.100332
[11] Yang, S., Sang, C., Hu, Y., & Wang, K. (2024). Coseismic and early postseismic deformation of the 2024 Mw7.45 Noto Peninsula earthquake. Geophysical Research Letters, 51, e2024GL108843. https://doi.org/10.1029/2024GL108843
[12] Malagnini, L., F. P. Lucente, P. De Gori, A. Akinci, and I. Munafo' (2012), Control of pore fluid pressure diffusion on fault failure mode: Insights from the 2009 L'Aquila seismic sequence, Journal of Geophysical Research, 117, B05302, https://doi.org/10.1029/2011JB008911